Alumina scale buckling during high temperature oxidation of Cr2AlC MAX Phase

A. Zuber, G. Parry, C. Coupeau, P.O. Renault, V. Gauthier-Brunet, S. Dubois

Alumina scale buckling during high temperature oxidation of Cr_2AlC MAX Phase

A. Zuber[1*], G. Parry[2], C. Coupeau[1], P. O. Renault[1], V. Gauthier-Brunet[1] and S. Dubois[1]

[1] Institut PPRIME, CNRS/Université de Poitiers/ENSMA, UPR 3346, TSA 41126, 86073, Poitiers Cedex 9, France.

[2] SIMAP - Grenoble INP Phelma 1130 rue de la Piscine, BP75 38402 Saint Martin d'Hères Cedex France

*corresponding author email address: axel.zuber@univ-poitiers.fr

Abstract

Single-crystal and fine-grained polycrystalline samples of Cr_2AlC were oxidized under dry air flow at temperature in the 1000-1400°C range during 100 h. A continuous alumina layer forms on top of the Cr_2AlC surface whereas a Cr_7C_3 sublayer also appears. In-lab characterization of oxidized Cr_2AlC samples shows strong damaging at the free surface, resulting from the buckling of the alumina scale. In-situ X-ray diffraction measurements under synchrotron radiations were performed to measure the lattice strain during the first hours of oxidation process and further calculate the internal stress in the Al_2O_3 layers. Alumina layers undergo tensile stress during isothermal oxidation, showing that the buckling of the alumina scale does not result from the oxide growth. Such a tensile stress likely results from the Cr_2AlC to Cr_7C_3 phase transformation. During cooling, the tensile stress decreases down to compressive values, due to the thermal expansion coefficient mismatch between the film and the substrate, leading to buckling of the alumina layer. It is demonstrated that the dimensions of the buckles cannot be explained either by gas pressure or by the magnitude of the internal compressive stress in the alumina scale after cooling. The discrepancy between the experimental maximum deflection and the one predicted by the elastic theory can only be explained by a significant plastic deformation occurring in the alumina scale.

Keywords:

Cr_2AlC, high-temperature oxidation, microstructure, single crystal, buckling, finite-element

1. Introduction

Among high-temperature materials, the family of MAX phases (M transition metal, A p-bloc element, X carbon or nitrogen) offers, besides ceramic and metallic mixed properties, a variety of oxidation resistant materials [1, 2, 3]. Due to the nanolamellar structure of the MAX phases and the weak bonding between its M_6X octahedrons sheets and planes of A element, the nature of the A element governs the nature of the oxide scale that forms during oxidation. As an example, M-Al-X phases are known as alumina-forming materials even if some M_xO_y oxides can be formed [4]. Ti_2AlC and Cr_2AlC are the most promising of them and their oxidation resistance has been assessed multiple times [5- 8]. Both of them form continuous alumina layer whose integrity is a key element for a protective oxide scale - Cr_2AlC also forms a Cr_7C_3 sublayer. The adherence of protective oxide scales to MAX substrate is governed by the stored elastic energy in the scale which drives delamination and fracture toughness of the MAX/oxide interface. Any modifications of the MAX or the exposure environments which decreases the former or increases the later will improve the durability of the system. The oxide scale integrity is often manhandled by stresses developing during its formation or cooling [9]. The stress state in the oxide scale may result from different origins, such as phase transformation, oxide growth, thermal expansion mismatch between the oxide and the MAX (thermal stresses) and any stress relaxation which can result from creep of the oxide or the MAX cracking, delamination, buckling of the oxide layer. Hou *et al.* have demonstrated using *in situ* X-Ray diffraction (XRD), that the alumina scale formed onto Fe28Al and Fe40AlHf alloys undergoes tensile stress (in the range 100-200 MPa). Indeed, volume contraction (in the range 5-8%) resulting from the transformation of transition alumina (either θ or γ) to the α form leads to an α-Al_2O_3 in tension. For other compositions of Fe or Ni-based alloys, alumina scale may undergo a compressive stress during its growth, which is relaxed by wrinkling or buckling [10, 11]. In the case of FeCrAl and NiAl alloys or Ti_2AlC MAX phase, the oxide scale demonstrates to buckle supposedly due to the lateral growth of the alumina grains and subsequent increasing compressive stress [12-16]. The alumina film may then delaminate and buckle from its substrate [17-19]. In the case of Ti_2AlC, the breakaway oxidation phenomenon [16], which consists in the nucleation of TiO_2 rutile under the buckles, damages irrevocably the alumina scale. This problem is not a concern with Cr_2AlC, since the chromium carbide beneath the alumina scale oxidizes slowly by carbon volatilization before forming chromia which is also a quite protective oxide scale. Still, cracking and buckling of the alumina scale formed on Cr_2AlC were reported in recent studies but their origin remains unclear [20].

This paper focuses on the alumina buckles formed during Cr_2AlC oxidation and their origin. Several in-lab characterizations, among which *in situ* X-ray diffraction using synchrotron facilities, interferometric microscopy and scanning electron microscopy with focalized ion beam, were carried out to quantify the mechanical state of the alumina scales. The experimental results are compared to finite elements simulations and discussed in the framework of the elastic theory to understand the occurrence of such buckles in alumina scales.

2. Experimental details

Synthesis of polycrystalline fine-grained Cr_2AlC samples, as well as single crystals, are described in reference [20]. The fine-grained samples have few (<4 vol.%) impurities of alumina and Cr_7C_3 with a grain size of about 2 µm [20]. The single-crystals are highly pure plates of about a square centimeter. The basal plane of the nanolamellar Cr_2AlC structure is oriented parallel to the plate.

The polycrystalline and single crystal samples were cut into parallelepipeds (10x2x2 mm^3) and equilateral triangles (~0.5 cm and a few microns in thickness), respectively. Both were polished with silicon carbide abrasive disks and finished on felt disk with diamond paste of 0.25 µm particles. The polished samples were placed into a thermogravimetric analysis chamber (TGA, SETARAM EVOSYSTEM) and heated under Ar flow at 20°C/min; TGA curves are not shown in this manuscript [see 20]. The subsequent isothermal oxidation treatment was performed under dry air flow in the 1000-1400°C temperature range during 100 h before cooling at 20°C/min.

The mean lattice strain evolution of alumina was monitored by *in situ* synchrotron X-Ray diffraction for both single-crystals and fine-grained samples during the oxidation and cooling processes. It has to be note that, in the case of single crystals, only the surface parallel to the basal plane is submitted to the X-Ray beam. The

samples were placed on the high-quality goniometer of BM02 beamline at the European Synchrotron Research Facility (Grenoble, France) [21] inside the multipurpose QMAX furnace [22]. The QMAX furnace allows oxidizing the samples at 1150 °C for 6-9 hours under dry air in a closed beryllium dome. Heating rate of 10°C/min was performed under an Ar atmosphere to avoid the formation of transition alumina on the surface. Once the set temperature was reached, a flow of dry air was introduced into the Be dome. Cooling was then carried out at a controlled rate of 10°C/min still under dry air. The standard beam size of 0.3x0.3 mm² was used with an energy of 20 keV and an incident angle of Ω=10°. XRD diagrams were recorded using 2D D5 detector that is large enough to get sufficient part of the Debye-Scherrer rings to extract the stress evolution in the oxide layer during its formation. The internal stresses in the Al_2O_3 crystalline layers were subsequently determined using the $\sin^2(\Psi)$ method [23].

3. Finite element simulation details

Finite element modelling (FEM) simulations, using the Abaqus software [24] have been carried out to simulate the deformation of the observed buckles. The model is developed in a 2D axisymmetric framework. The geometry, loading and boundary conditions are depicted in the insert in Fig. 7. The radius of the studied buckle is fixed to R=25.5 μm, its thickness to h=5 μm, in agreement with the characteristic buckle presented hereafter in Fig. 8. The origin of the reference frame is denoted O; e_r and e_z are the unit vectors of the radial and vertical directions, respectively. The displacement components along e_r and e_z are respectively denoted u and w, for any point M(r,z) of the domain. The substrate surface is lying along the line z=0. The bottom surface of the film is initially located along z=0 and its top surface along z=h. The film is modelled as a linear elastic body, while the substrate is represented by a rigid line. The following boundary conditions are imposed during all the simulation: $\forall\, M$ such that r=R (*i.e.* along the edge of the buckle at the delamination front), u=w=0. A rigid contact is used between the bottom of the film and the underneath rigid line (substrate), forbidding the displacement of the film in the lower half-space (unilateral contact condition).

The buckle is a post-critical buckled structure characterized by large values of the out-of-plane displacement component w, such that the calculations must be carried out within the framework of large displacement hypothesis using the Green-Lagrange strain tensor. The calculation consists of three successive loading steps. Step 1: geometrical defect induced by a small pressure (0.1 MPa) applied on the lower part of the film (z=0). This induces a very small deflection of the plate, that will be useful in the following step in order to trigger buckling. Step 2: Application of the internal stress: a uniform compression stress, of intensity σ_0, is generated inside the film. In order to do so, a thermal dilatation strain ε_0 ($\varepsilon_0 > 0$) is imposed to the film, in order to mimic the eigenstrain associated to the oxidation growth process. As the displacement is blocked in the radial direction of the initially planar film, the eigenstrain ε_0 generates a compressive stress in the film. Indeed, the total strain, which is the sum of the thermal and elastic strains, vanishes, such that $\sigma_{rr} = \sigma_{\vartheta\vartheta} = E.\varepsilon_0 /(1-\nu^2) = -\sigma_0$ and $\sigma_{r\vartheta} = 0$). If σ_0 becomes larger than the critical buckling load, buckling occurs, characterized by an increase of the buckle maximum deflection. Note that the eigenstrain generated during this step is maintained during the next step. Step 3: A uniform pressure P is applied onto the lower surface of the film. Leading to further increase of the buckle deflection. Biquadratic 8-nodes axisymmetric quadrilateral elements with reduced integration, are used to mesh the film (CAX8R according to Abaqus elements library). A quasi-static analysis is carried out using the implicit solver (ABAQUS Standard).

4. Results and discussion

Buckling of the alumina scale is observed both on single crystals after oxidation at 1400 °C for 100 hours (Fig. 1A) and on polycrystalline fine-grained samples above 1000 °C for the same oxidation time (Fig. 1B). A more advanced damaging state of the film is identified on the polycrystals compared to the quite isolated buckles observed on the single crystals. Some parts of the oxide scale spalled likely due to cracking/delamination from sample handling. Such a difference in damaging may be explained by the oxide scale thickness. Indeed, it has been demonstrated that the oxide growth is slower on the basal plane of the

single crystal than on the polycrystalline samples [20]. Grain boundaries may also play a key role in the interfacial delamination prior to buckling. Additionally, the adhesion energy of the alumina scale on the carbide likely depends on the orientation of the carbide grains.

Two major diffraction peaks of the α-alumina, (104) and (110) peaks of the R$\bar{3}$c space group, have been examined during oxidation using *in situ* synchrotron XRD. The evolution of the integrated area of the alumina (104) and (110) peaks are shown in Fig. 2 during the oxidation at 1150°C of Cr_2AlC single crystal and polycrystalline samples. The integrated area increases with time for both samples but in very different ways. On the single crystal, the alumina scale grows very slowly as reported in Fig. 2A; the diffusion-limited oxidation regime is not reached after 6 hours of oxidation [20]. On the other hand, the growth is faster on the polycrystal and follows a power law, as shown in Fig. 2B. The power law shaped curve observed with the polycrystalline sample well agrees with the mass gain curves obtained during oxidation of Cr_2AlC and results from diffusion of oxygen atoms through the alumina grain boundaries [20, 25].

The stress evolution of the alumina layers during the isothermal oxidation at 1150°C of the single-crystal and fine-grained polycrystalline samples is shown in Fig. 3. The two layers are in tension, with a stress magnitude of few hundreds of MPa. Note that the single-crystal data are more scattered due to the low intensity of the XRD peaks. The tensile stress decreases with time on the single crystal (Fig. 3A) whereas no significant stress evolution is observed during the alumina scale growth on top of the polycrystalline sample (Fig. 3B). Such a difference in tensile stress evolution is unclear but it may result from the large difference in oxidation rate. The tensile stress of the alumina layer is quite typical of phase transformation stresses [10, 11]: it can be due either to θ to α alumina phase transition (at the first stage of oxidation) or to the Cr_2AlC to Cr_7C_3 phase transformation. It can be note that transition alumina's (γ, δ or θ) have not been detected by XRD. In order to explain the development of buckled alumina on iron-chromium-aluminum alloys, it has been proposed that inward oxygen diffusion through the oxide grain boundaries is accompanied by outward bulk diffusion of aluminum in the alumina grains [18, 19]. Reaction between the inward- and outward-diffusing species results in the formation of alumina within the existing oxide layer, the reaction taking place in the region of the oxide grain boundaries. Consequently, in addition to general thickening, lateral growth of the oxide occurs as oxidation proceeds, leading to compressive stresses and alumina scale buckling. Nevertheless, such compressive stresses have never been observed on our oxidized Cr_2AlC samples. One has to note that the transformation of Cr_2AlC into Cr_7C_3 results in a quite large volume variation (3 volumes of a Cr_2AlC cell only correspond to about one third of the Cr_7C_3 cell volume). As a result, the transformation of Cr_2AlC into Cr_7C_3 leads to tensile stresses on the upper alumina layer, in good agreement with XRD results.

The stress evolution of the Al_2O_3 layers during the further cooling is shown in Fig. 4. The alumina tensile stress decreases to reach a compressive stress of -1.4 ± 0.1 GPa at RT. Such a compressive stress value is significantly lower than the thermal stress given by:

$$\sigma_{th}=\left(\frac{E_{Al203}}{1-\nu_{Al203}}\right).\Delta\alpha.\Delta T = -2.8 \text{ GPa}, \quad (1)$$

where Δα is the thermal expansion coefficient mismatch and ΔT is the temperature difference between 1200°C and 20°C, with $E_{Al_2O_3}$= E_f = 390 GPa at room temperature [26], $\nu_{Al_2O_3}$ = ν_f = 0.27, $\alpha_{Al_2O_3}$= 8.1 10^{-6} K^{-1} and α_{Cr_2AlC} = 12.6 10^{-6} K^{-1} [27-29]. The discrepancy may be explained by creep/stress relaxation at high temperature upon cooling or by the elastic modulus that can significantly differ from a thermally growth oxide scale and a bulk material [30].

The circular alumina buckles have been morphologically determined with the help of a white light interferometer (Talysurf CCI), as observed in Fig. 5A. A characteristic profile of a buckle observed on single crystals oxidized at 1400°C for 100h is shown in Fig. 5B. The maximum deflection δ and radius R were estimated to be 12 µm and 23 µm, respectively. Note that the buckles exhibit plenty of needles, as observed on the SEM micrograph of Fig. 5C, which explains the rough profile observed in Fig. 5B.

The buckling of thin films and coatings have been extensively studied by the past, especially in the framework of the Föppl-Von Kármán equations [31, 32]. Assuming an isotropic elastic film and an infinitely rigid substrate, the critical stress for buckling to occur is given in an axisymmetric configuration by [33]:

$$\sigma_c = 1{,}2235.\frac{E_f}{1-\nu_f^2}.\left(\frac{h}{R}\right)^2, \quad (2)$$

with E_f the Young's modulus of the film, ν_f its Poisson's ratio, h the film thickness and R the radius of the circular delaminated area at the interface. Note that the equation may differ depending on the 1D (straight-sided buckle) or 2D (circular buckle) model. σ is here given positive in compression for convenience.

For a compressive stress $\sigma > \sigma_c$, an approximation of the maximum deflection of the film δ is given by [33]:

$$\frac{\delta^2}{h^2} = \frac{1}{c_1}\left[0.8173.\sigma.\frac{1-\nu_f^2}{E_f}.\left(\frac{R}{h}\right)^2 - 1\right], \quad (3)$$

with $c_1 = 0.2473(1+\nu_f) + 0.2231(1-\nu_f^2)$.

The morphological parameters δ^2 and R^2 of various circular buckles observed on single crystals oxidized at 1400°C for 100h have been reported in Fig. 6. Assuming a compressive stress σ = 1.4 GPa as determined by XRD, the evolution of δ^2 as a function of R^2 expected by Eq. (2) has been superimposed in Fig. 6. Noting the logarithmic scale for δ^2, the experimental deflections are shown to be strongly higher than the ones expected by the elastic theory.

The elasticity of the substrate (with respect to the one of the film) was shown to significantly modify both Eqs. (2) and (3) [34]. The elastic contrast between the elasticity of the film and the substrate can be characterized by the Dundurs' coefficient α given by:

$$\alpha = \frac{E_{f/(1-\nu_f^2)} - E_{s/(1-\nu_s^2)}}{E_{f/(1-\nu_f^2)} + E_{s/(1-\nu_s^2)}}. \quad (4)$$

α=-1 (*resp*. α=+1) corresponds to the case of a compliant film on a stiff substrate (*resp*. a stiff film on a compliant substrate). α=-1 is thus related to the case of the Föppl-Von Kármán equations. As α is increased, the critical stress for buckling is decreased and the maximum deflection δ is increased. In the case of straight-sided buckle, the two Eqs. (2) and (3) were thus refined by two correcting factors $\gamma_{\sigma c}$ and γ_δ [34]. In our case of an Al_2O_3/Cr_2AlC system for which $E_{Cr_2AlC} = E_s$ = 351 GPa and $\nu_{Cr_2AlC} = \nu_s$ = 0.20 [35], α was estimated to be equal to 0.07. From reference [34], the two correcting parameters were found to be 0.92 and 1,10, respectively. Taking into account the elasticity of the substrate, the refined evolution of δ^2 versus R^2 has been plotted as a dotted line in Fig. 6. It shows once again the discrepancy between the refined elastic model and the experimental results. Note that the refinement was performed in the case of a 1D model [34]; it is however believed that a 2D refinement would not succeed to compensate for the huge discrepancy observed in Fig. 6.

It is emphasized that the morphology of a buckle may result from either a compressive stress or an internal pressure between the inside and outside parts of the film (or any combination between). Such a pressure may result from volatile gas, such as carbon oxide gaseous species produced during the oxidation of the chromium carbide layer. To explore such a statement, finite element simulations were performed to estimate the gas pressure necessary to reach our experimental maximum deflection δ. A characteristic buckle with dimensions R = 45 µm and δ = 17 µm has been chosen as an example. The gas pressure P is shown in Fig. 7 as a function of δ, for various σ. First, assuming no compressive stress (σ=0), it shows that a gas pressure of more than P=35 GPa is expected to obtain the δ =17 µm value experimentally observed, which is not realistic. It is also shown that, even with a compressive stress of σ = 2 GPa (close to the one experimentally determined), no significant decrease of the necessary gas pressure is observed; additionally, a non-realistic compressive stress of σ = 25 GPa would result in even a gas pressure of at least P=30 GPa. These numerical results strongly suggest that the alumina buckles cannot be explained by an internal pressure. To confirm such a conclusion, *i.e.* no accumulation of gas below the alumina scale, some buckles have been opened to atmospheric pressure by a focused ion beam (FIB) technique. A characteristic circular buckle was observed by SEM and finely characterized by a white light interferometry technique, before and after the FIB cut (Fig. 8). In case of a gas pressure below the buckle, the FIB cut should result in a decrease of the maximum deflection δ [36]. No significant change of the buckle profile was observed before (Fig. 8A) and after (Fig. 8B) the FIB cut, demonstrating no gas accumulation below the Al_2O_3 scale.

The dimensions of the circular buckles cannot be explained by a gas pressure, no more by the magnitude of the internal compressive stress in the alumina scale after cooling. The elasticity of the substrate does not bring more explanations. As previously mentioned, the Eqs. (2) and (3) are only valid in the framework of the elastic theory. The discrepancy between the buckling model and the experimental data can only be explained by a significant plastic damage occurring in the alumina scale. Note that such plastic events resulting from the buckling-induced delamination have already been reported in the literature [37-39].

4. Conclusion

Using in situ synchrotron X-Ray diffraction during oxidation process, it is demonstrated that the alumina growth on top of Cr_2AlC is accompanied by tensile stress of the alumina scale. Such a result differs from the one discussed by Stött *et al.* [17, 18] who showed that alumina scale is submitted to compressive stress during its growth on top of iron-chromium-aluminum alloys. It is believed that compressive stresses result from the formation of oxide within the existing oxide layer by reaction between oxygen diffusing inward through the oxide grain boundaries and aluminum diffusing outward through the bulk oxide. Although it has been demonstrated by different authors [15, 16] that the aluminum oxide formation mechanism on top of Cr_2AlC is the one described by Stött *et al.*, it fails to explain the tensile stress of the alumina scale measured in this study. As the transformation of Cr_2AlC into Cr_7C_3 results in a quite large volume variation (3 volumes of a Cr_2AlC cell only correspond to one third of the Cr_7C_3 cell volume), the phase transformation of Cr_2AlC into Cr_7C_3 leads to tensile stress on the upper alumina layer, which is in compatible agreement with our reported tensile stresses.

During cooling, the alumina layer is submitted to a compressive stress as a result of the shrinkage of both Cr_2AlC substrate and Cr_7C_3 sublayer. The measured compressive stress of 1.4 GPa experimentally determined by XRD is lower than the calculated thermal stress resulting from the cooling (2.8 GPa), but is relevant to explain the buckling, since in compression. However, the dimensions of the circular buckles cannot be explained by the level of the internal compressive stress in the alumina scale. Moreover, it has been demonstrated that a gas pressure that may result from the carbon oxide formation due to the oxidation of the chromium carbide layer [25] cannot better explain these dimensions. All these results strongly suggest that a significant plastic deformation of the alumina scale is likely to occur during the buckling-induced delamination in order to account for the dimensions of the buckles experimentally observed.

5. Acknowledgement

Special thanks to the Région Nouvelle-Aquitaine and the Ministère de l'Enseignement Supérieur et de la Recherche for funding this research. This work was supported by the French government program “Investissements d’Avenir” (EUR INTREE, reference ANR-18-EURE-0010 and LABEX INTERACTIFS, reference ANR-11-LABEX-0017-01). This work was also supported by the European commission through the Horizon 2020 project IL TROVATORE (n° 740415). The authors also thank J. Gonzales-Julian and T. Ouisse for providing Cr_2AlC samples and R. Guinebretière for fruitful discussion. We acknowledge the ESRF and the French Collaborating Research Group (F-CRG) for provision of synchrotron radiation beamtimes and, M. Dupraz and A. Stephan (BM02) for their assistance.

6. References

[1] M.W. Barsoum. The $M_{n+1}AX_n$ phases: A new class of solids: Thermodynamically stable nanolaminates. Progress in Solid State Chemistry, volume 28, pp. 201–281, 2000. https://doi.org/10.1016/S0079-6786(00)00006-6

[2] D. J. Tallman, B. Anasori, M. W. Barsoum. A critical review of the oxidation of Ti2AlC, Ti3AlC2 and Cr2AlC in air. Materials Research Letters, volume 1, no. 3, pp. 115–125, 2013. http://dx.doi.org/10.1080/21663831.2013.806364

[3] M. Sokol, V. Natu, S. Kota, M.W. Barsoum. On the chemical diversity of the max phases. Trends in Chemistry, 1:210–223, 2019. https://doi.org/10.1016/j.trechm.2019.02.016

[4] M. Magnuson, M. Mattesini. Chemical bonding and electronic-structure in MAX-phases as viewed by X-Ray spectroscopy and density functional theory. Thin Solid Films, volume 621, pp.108–1300, 2017. http://dx.doi.org/10.1016/j.tsf.2016.11.005

[5] D. B. Lee, T. D. Nguyen, S. W. Park. Long-time oxidation of Cr2AlC between 700 and 1,000 °C in air. Oxidation of Metals, volume 77, no. 5, pp. 275–287, 2012. http://dx.doi.org/10.1007/ s11085-012-9285-7. 188.

[6] S. Li, L. Xiao, G. Song, X. Wu, W. G. Sloof, S. van der Zwaag. Oxidation and crack healing behavior of a fine-grained Cr2AlC ceramic. Journal of the American Ceramic Society, volume 96, no. 3, pp. 892–899, 2013. http://dx.doi.org/10.1111/jace.12170.

[7] Z. J. Lin, M. S. Li, J. Y. Wang, and Y. C. Zhou. Influence of Water Vapor on the Oxidation Behavior of Ti3AlC2 and Ti2AlC. Scripta Materialia, volume 58, pp. 29–32, 2008. http://dx.doi.org/10.1016/j.scriptamat.2007.09.011.

[8] H. P. Zhu, X. K. Qian, H. Y. Wu, J. Lei, Y. C. Song, X. D. He, and Y. Zhou. Cyclic Oxidation of Ternary Layered Ti2AlC at 600-1000°C in Air." International Journal of Applied Ceramic Technology, volume 12, p. 403, 2015. http://dx.doi.org/10.1111/ijac.12182.

[9] D. L. Douglass, P. Kofstad, P. Rahmel, G. C.Wood. International workshop on high-temperature corrosion. Oxidation of Metals, volume 45, no. 5, pp. 529–620, 1996. http://dx.doi.org/10.1007/BF01046850

[10] P. Y. Hou, A. P. Paulikas, B. W. Veal. Growth strains and stress relaxation in alumina scales during high temperature oxidation. Materials Science Forum, volume 461-464, pp. 671–680, 2004. http://dx.doi.org/10.4028/www.scientific.net/MSF.461-464.671

[11] P. Y. Hou, A. P. Paulikas, B. W. Veal. Growth strains in thermally grown Al2O3 scales studied using synchrotron radiation. JOM, volume 61, no. 7, pp. 51–55, 2009. http://dx.doi.org/10.1007/s11837-009-0103-x.

[12] F. N. Rhines, J. S. Wolf. The role of oxide microstructure and growth stresses in the high temperature scaling of nickel. Metallurgical Transactions, volume 1, no. 6, pp. 1701–1710, 1970. http://dx.doi.org/10.1007/BF02642020

[13] D. M. Lipkin, H. Schaffer, F. Adar, D. R. Clarke. Lateral growth kinetics of α-alumina accompanying the formation of a protective scale on (111) NiAl during oxidation at 1100 °C. Applied Physics Letters, volume 70, no. 19, pp. 2550–2552, 1997. http://dx.doi.org/10.1063/1.118917

[14] C. Sarioglu, M. J. Stiger, J. R. Blachere, R. Janakiraman, E. Schumann, A. Ashary, F. S. Pettit and G. H. Meier, The adhesion of alumina films to metallic alloys and coatings, Materials and Corrosion, volume 51, pp. 358-372, 2000. https://doi.org/10.1002/(SICI)1521-4176(200005)51:5<358::AID-MACO358>3.0.CO;2-C

[15] J. Sniezewski, P. Lours, Y. Le Maoult. Buckling and spalling failure of alumina grown by oxidation on FeCrAl alloys. Materials at High Temperatures, volume 28, no. 1, pp. 17–20, 2011. http://dx.doi.org/10.3184/096034011X12962385894289.

[16] S. Badie, D. Sebold, R. Vaßen, O. Guillon, J. Gonzalez-Julian. Mechanism for breakaway oxidation of the Ti2AlC MAX phase. Acta Materialia, volume 215, pp. 117025, 2021. http://dx.doi.org/10.1016/j.actamat.2021.117025

[17] A. Golightly, F. H. Stött, and G. C. Wood. The Influence of Scale Adhesion Alloy Yttrium Additions on the Oxide to an Iron-Chromium-Aluminum Alloy, Oxidation of Metals, Vol. 10, n°3, 163-187, 1976. https://doi.org/10.1007/BF00612158

[18] A. Golightly, F. H. Stött, and G. C. Wood. The Early Stages of Development of 6e-A1203 Scales on Fe-Cr-AI and Fe-Cr-AI-Y Alloys at High Temperature. Oxidation of Metals, Vol. 14, n°3, 217-234, 1980. https://doi.org/10.1007/BF00604565

[19] F. H. Stott, G. C. Wood. Growth and adhesion of oxide scales on Al2O3 forming alloys and coatings. Materials Science and Engineering, volume 87, pp. 267–274, 1987. http://dx.doi.org/10.1016/0025-5416(87)90388-0

[20] A. Zuber, V. Gauthier-Brunet, J. Roger, J. Gonzalez-Julian, T. Ouisse, S. Dubois. Towards a better understanding of the high-temperature oxidation of MAX phase Cr_2AlC. Journal of the European Ceramic Society, volume 42, issue 5, p. 2089-2096, 2022. https://doi.org/10.1016/j.jeurceramsoc.2021.12.057.

[21] Gilbert André Chahine, Nils Blanc, Stephan Arnaud, Frédéric de Geuser, René Guinebretière, et al.. Advanced Non-Destructive in Situ Characterization of Metals with the French Collaborating Research Group D2AM/BM02 Beamline at the European Synchrotron Radiation Facility. Metals, volume 9, issue 3, p.352, 2019. http://dx.doi.org/10.3390/met9030352.

[22] R. Guinebretière, S. Arnaud, N. Blanc, N. Boudet, E. Thune, D. Babonneau, O. Castelnau. Full reciprocal-space mapping up to 2000 K under controlled atmosphere: the multipurpose QMAX furnace. Journal of Applied Crystallography, volume 53, pp. 650–661, 2020. https://doi.org/10.1107/S160057672000432X.

[23] V. Hauk, Structural and Residual Stress Analysis by Non-destructive Methods: Evaluation - Application - Assessment, Elsevier Science, 1997. ISBN: 9780080541952.

[24] Abaqus Manuals Collection, Dassault Systems; Simulia Corp., Providence, RI, USA, 2013.

[25] A. Zuber, V. Gauthier-Brunet, J. Roger, J. Gonzalez-Julian, T. Ouisse, S. Dubois. Cr_2AlC high temperature oxidation under dry and wet air: Understanding of the oxidation mechanism, Journal of the European Ceramic Society, volume 43, issue 12, p. 5159-5167, 2023. https://doi.org/10.1016/j.jeurceramsoc.2023.05.012

[26] R. G. Munro, Elastic Moduli data for polycrystalline oxide ceramics, Ceramics division, National Institute of Standards and Technology, NIST 6853, 2002.

[27] B. S. Mitchell. An Introduction to Materials Engineering and Science: For Chemical and Materials Engineers. 2003. http://dx.doi.org/10.1002/0471473359.

[28] T. H. Scabarozi, S. Amini, O. Leaffer, A. Ganguly, S. Gupta, W. Tambussi, S. Clipper, J. E. Spanier, M. W. Barsoum, J. D. Hettinger, and S. E. Lofland , "Thermal expansion of select $M_{n+1}AX_n$ (M=early transition metal, A=A group element, X=C or N) phases measured by high temperature x-ray diffraction and dilatometry", Journal of Applied Physics, volume 105, p. 013543, 2009. https://doi.org/10.1063/1.3021465.

[29] J. W. Hutchinson, M. Y. He, A. G. Evans. The influence of imperfections on the nucleation and propagation of buckling driven delaminations. Journal of the Mechanics and Physics of Solids, volume 48, no. 4, pp. 709–734, 2000. http://dx.doi.org/10.1016/S0022-5096(99)00050-2

[30] Y. Zou, L. F. Ge, Z.Y. Li, J.W. Guo, W. Zhu, Z.S. Ma, Determination of the intrinsic elastic modulus, hardness and fracture strength of thermally growth oxide by nanoindentation and tensile tests, Engineering Failure Analysis 131, 105815, 2022.

[31] A. Föppl. Vorlesungen über technische mechanik. volume 5, 1907.

[32] T.V. Kármán. Festigkeitsprobleme in maschinenbau, in “Encyclopadie der mathematischen wissenschaften”. chapter IV/4, pp. 311–385, 1910.

[33] J. W. Hutchinson, M. D. Thouless, E. G. Liniger. Growth and configurational stability of circular, buckling-driven film delaminations. Acta Metallurgica et Materialia, volume 40, no. 2, pp. 295– 308, 1992. http://dx.doi.org/10.1016/0956-7151(92)90304-W.

[34] G. Parry, J. Colin, C. Coupeau, F. Foucher, A. Cimetière, J. Grilhé, Effect of substrate compliance on the global unilateral post-buckling of coatings: AFM observations and finite element calculations, Acta Materialia 53, pp. 441–447, 2005. https://doi.org/10.1016/j.actamat.2004.09.039

[35] Z. Sun, S. Li, R. Ahuja and J. M. Schneider, Calculated elastic properties of M_2AlC (M = Ti, V, Cr, Nb and Ta). Solid State Commun., 129, 589–592, 2004.

[36] C. Coupeau, J. Grilhé, E. Dion, L. Dantas de Morais, J. Colin, Evidence of vacuum between buckled films and their substrates. Thin Solid Films, volume 518, p. 5233-5236, 2010. https://doi.org/10.1016/j.tsf.2010.04.026

[37] S. Hamade, J. Durinck, G. Parry, C. Coupeau, A. Cimetière, J. Grilhé, J. Colin. Effect of plasticity and atmospheric pressure on the formation of donut- and croissant like buckles, Physical Review E volume 91, p. 012410, 2015. https://doi.org/10.1103/PhysRevE.91.012410

[38] J. Colin, C. Coupeau, J. Grilhé, Plastic folding of buckling structures. Physical Review Letters, volume 99, p. 046101, 2007. https://doi.org/10.1103/PhysRevLett.99.046101

[39] J. Durinck, C. Coupeau, J. Colin, J. Grilhé. A stress relaxation mechanism through buckling-induced dislocations in thin films. Journal of Applied Physics, volume 108, p. 026104, 2010. https://doi.org/10.1063/1.345722.

Figure captions

Figure 1: SEM surface micrographs, in back-scattered mode, of A) single crystal and B) fine-grained polycrystalline samples oxidized during 100 hours at 1400 °C and 1100 °C respectively.

Figure 2: Evolution of the integrated area of the (104) and (110) alumina diffraction peaks during the oxidation at 1150 °C of a Cr_2AlC (A) single-crystal and (B) fine-grained polycrystal.

Figure 3: Stress evolution in the Al_2O_3 layer during isothermal oxidation at 1150 °C of Cr_2AlC A) single-crystal and B) fine-grained polycrystalline samples.

Figure 4: Stress evolution in the Al_2O_3 layer during cooling to RT of a Cr_2AlC single-crystal oxidized at 1150 °C. Stress evolution is measured on the surface parallel to the basal plane of the single crystal.

Figure 5: A) Interferometric microscopy surface mapping of the buckled surface of a Cr_2AlC single crystal oxidized at 1400 °C for 100h. B) Characteristic dimensions of the blister as obtained from buckle profile and C) SEM micrograph of an isolated alumina buckle.

Figure 6: Variation of δ^2 versus R^2 as determined from the characteristic dimensions of different buckles formed on top of the Cr_2AlC single crystal oxidized at 1400°C for 100h (blue circles). The black line corresponds to the expected variation of δ^2 from the Hutchinson model (see text) and the dotted line corresponds to the corrected variation of δ^2 considering the elasticity of the substrate (see text).

Figure 7: Gas pressure, determined from finite element calculation, needed to reproduce a characteristic buckle (R = 45 µm and δ = 17 µm) for 3 different values of the internal stress in the alumina scale.

Figure 8: SEM micrographs of a characteristic buckle after the FIB cut with the corresponding before and after profiles of the buckle determined by white light interferometric microscopy.

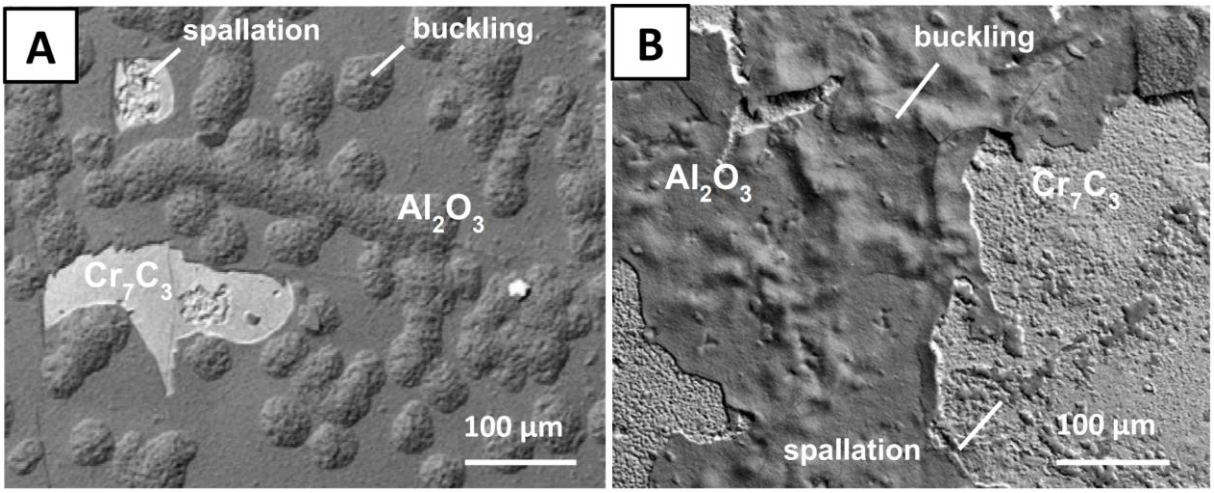
A
spallation
buckling
Al_2O_3
Cr_7C_3
100 µm
B
buckling
Al_2O_3
Cr_7C_3
spallation
100 µm

Figure 1

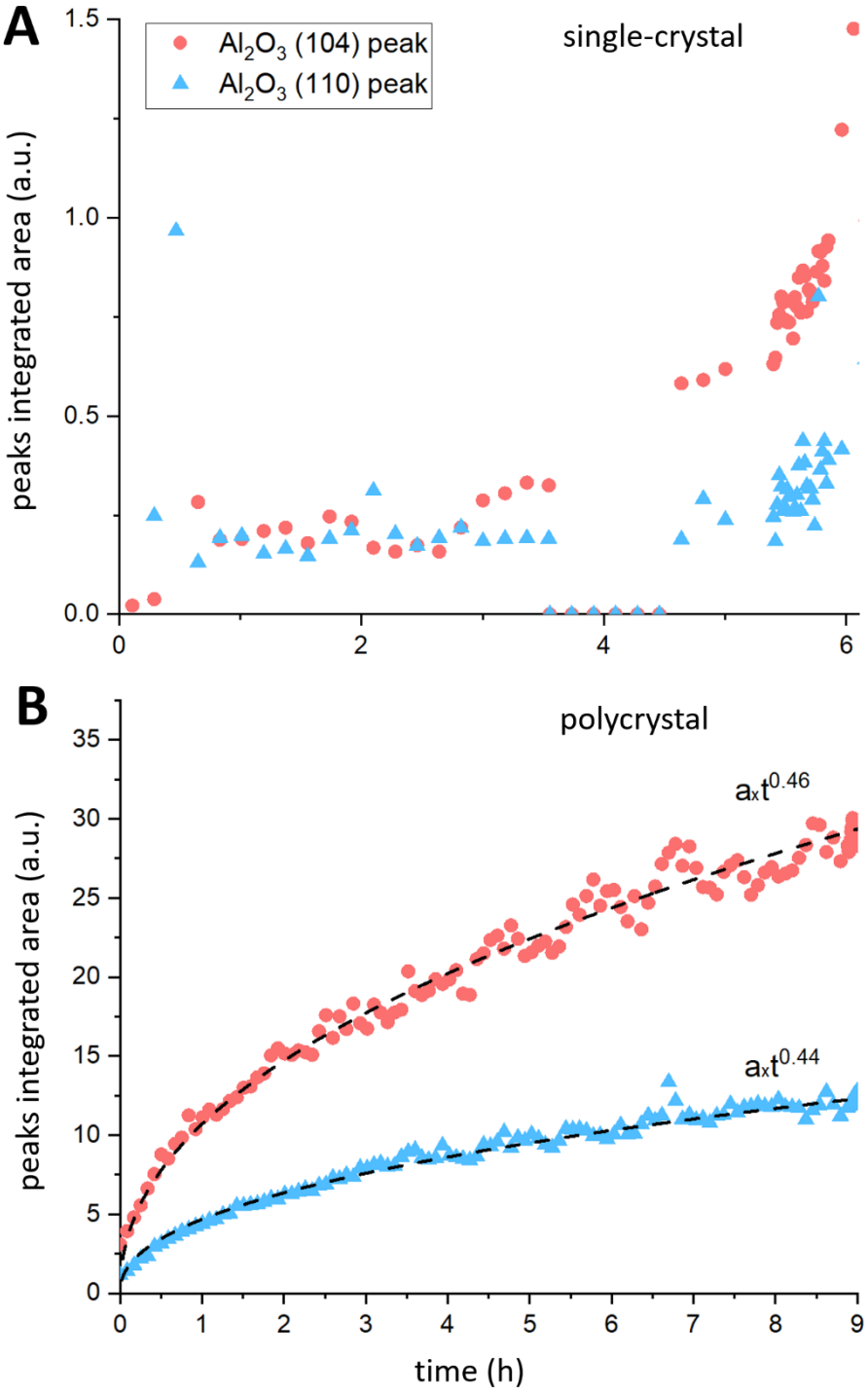
A
single-crystal
Al2O3 (104) peak
Al2O3 (110) peak
peaks integrated area (a.u.)
1.5
1.0
0.5
0.0
0
2
4
6
B
polycrystal
axt0.46
axt0.44
peaks integrated area (a.u.)
35
30
25
20
15
10
5
0
0
1
2
3
4
5
6
7
8
9
time (h)

Figure 2

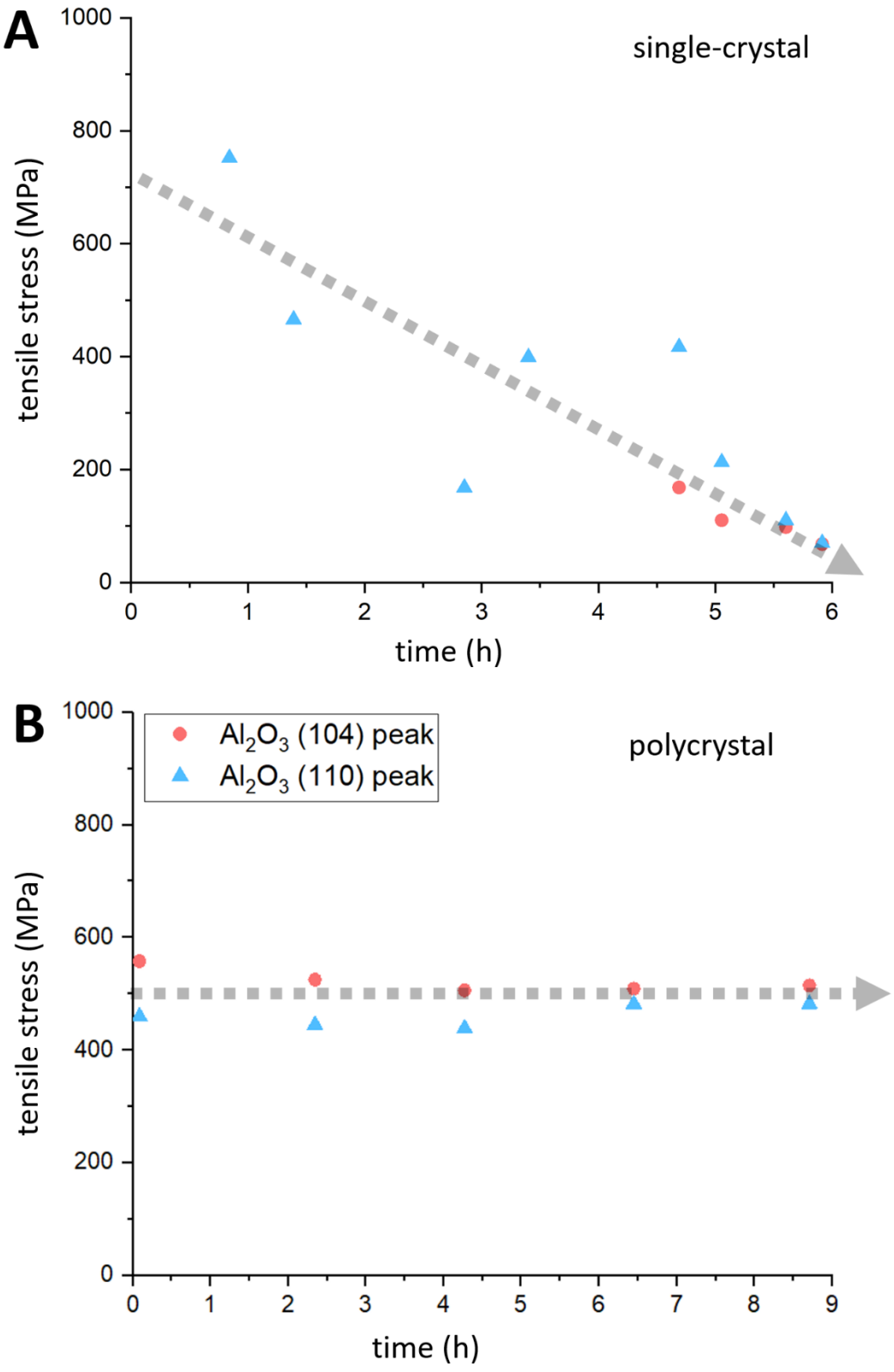
A
single-crystal
tensile stress (MPa)
time (h)
B
polycrystal
Al_2O_3 (104) peak
Al_2O_3 (110) peak
tensile stress (MPa)
time (h)

Figure 3

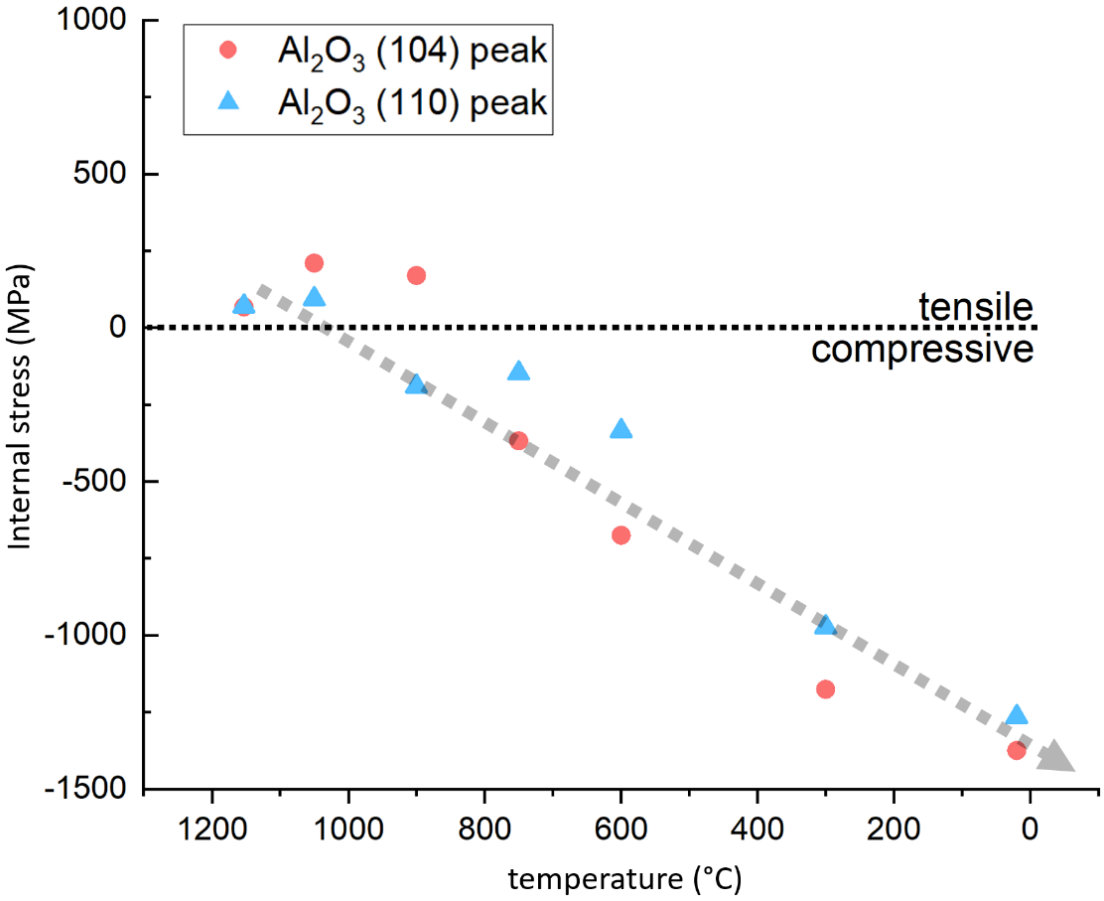
1000
500
0
-500
-1000
-1500
Internal stress (MPa)
Al2O3 (104) peak
Al2O3 (110) peak
tensile
compressive
1200
1000
800
600
400
200
0
temperature (°C)

Figure 4

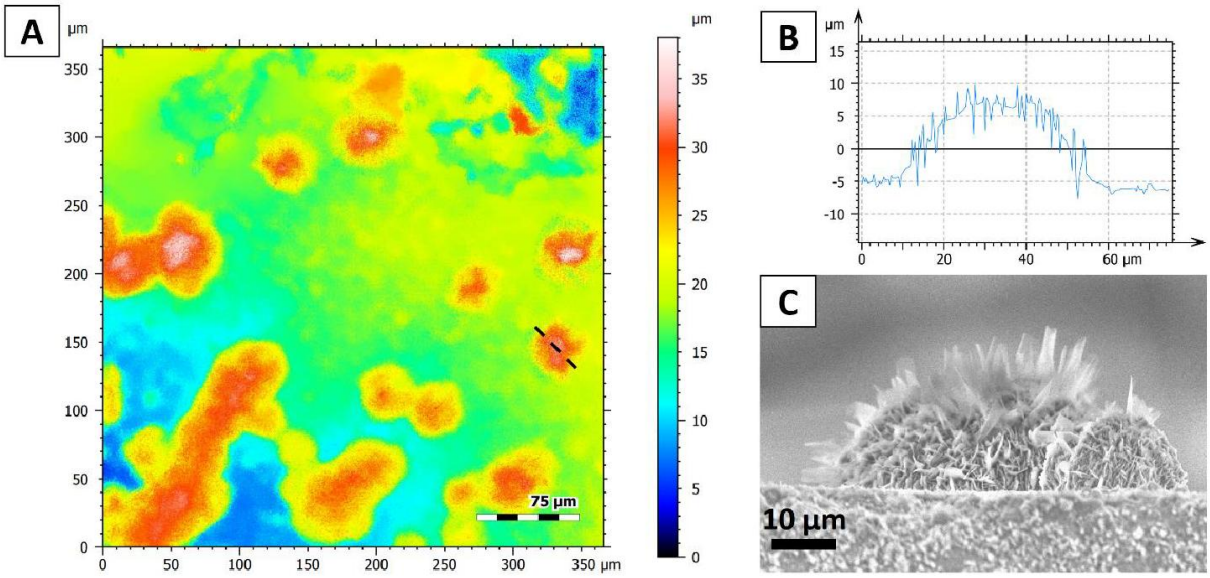
A
µm
350
300
250
200
150
100
50
0
0
50
100
150
200
250
300
350 µm
75 µm
µm
35
30
25
20
15
10
5
0
B
µm
15
10
5
0
-5
-10
0
20
40
60 µm
C
10 µm

Figure 5

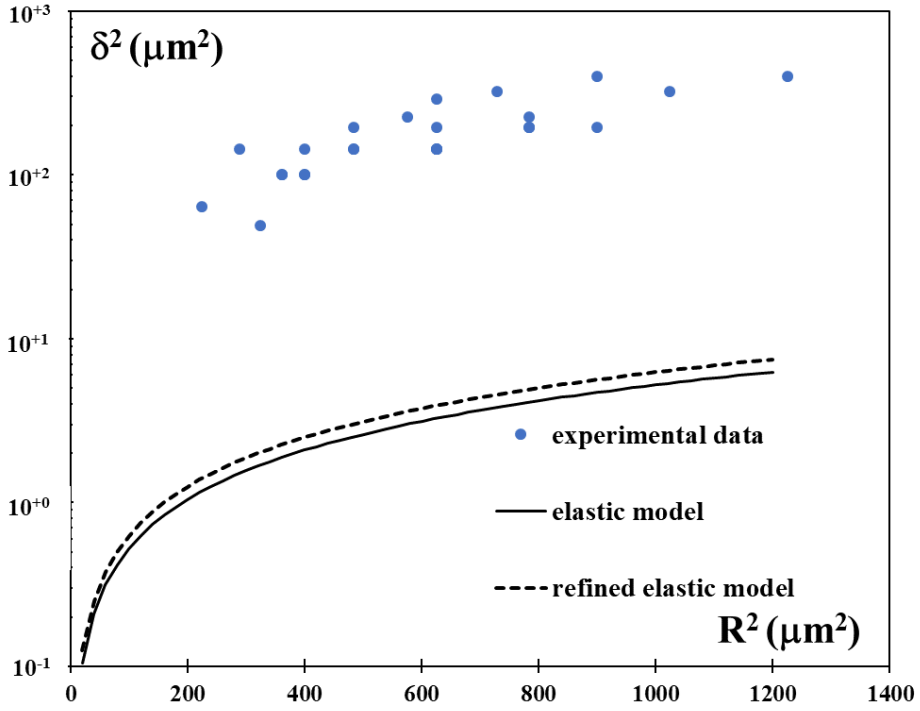
10^{+3}
δ^2 (μm^2)
10^{+2}
10^{+1}
10^{+0}
10^{-1}
0
200
400
600
800
1000
1200
1400
experimental data
elastic model
refined elastic model
R^2 (μm^2)

Figure 6

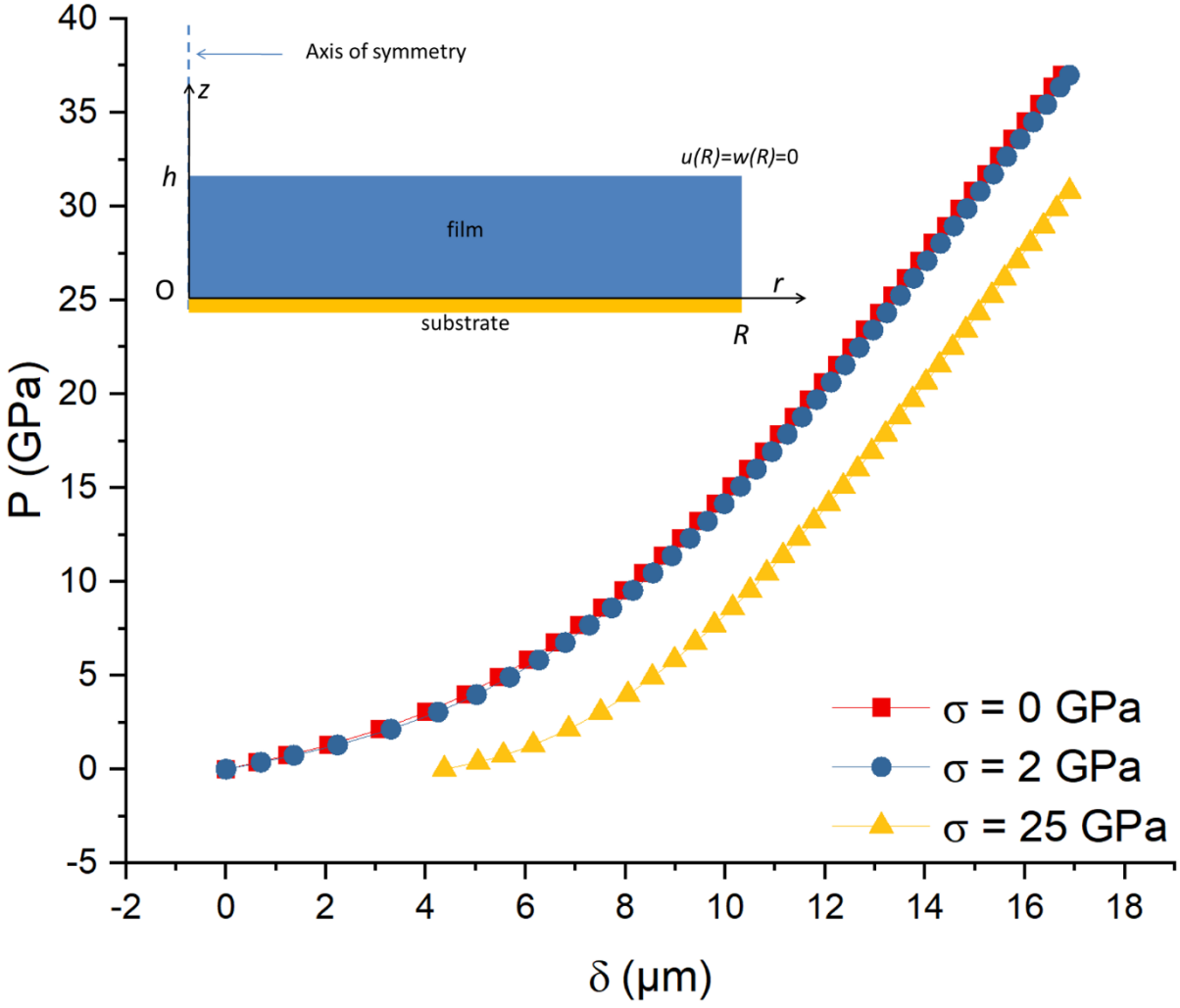
Axis of symmetry
z
h
u(R)=w(R)=0
film
O
r
substrate
R
P (GPa)
δ (μm)
σ = 0 GPa
σ = 2 GPa
σ = 25 GPa

Figure 7

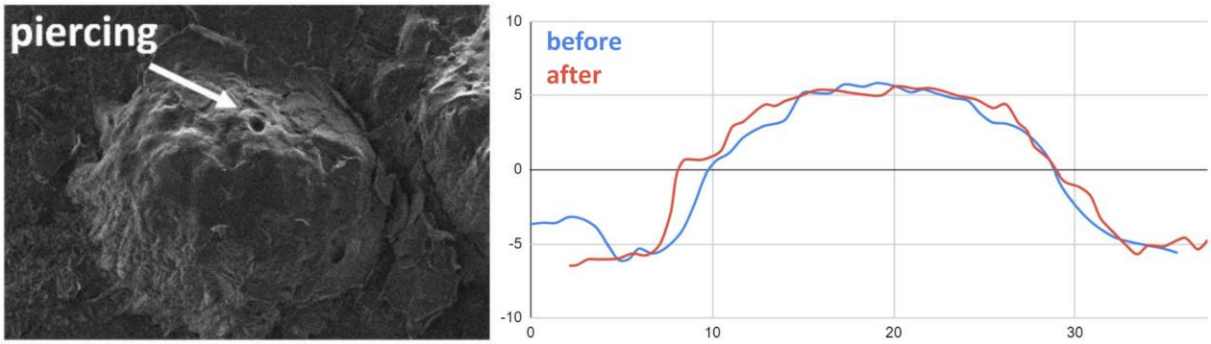

Figure 8